Mesoscale texture of cement hydrates

Katerina Ioannidou[a,b], Konrad J. Krakowiak[a], Mathieu Bauchy[c], Christian G. Hoover[a], Enrico Masoero[d], Sidney Yip[e], Franz-Josef Ulm[a], Pierre Levitz[f], Roland J.-M. Pellenq[a,b,g,1], and Emanuela Del Gado[h,1]

[a]Department of Civil and Environmental Engineering, Massachusetts Institute of Technology, Cambridge, MA 02139; [b]MultiScale Material Science for Energy and Environment, Massachusetts Institute of Technology–CNRS Joint Laboratory at Massachusetts Institute of Technology, Cambridge, MA 02139; [c]Department of Civil and Environmental Engineering, University of California, Los Angeles, CA 90095; [d]School of Civil Engineering and Geosciences, Newcastle University, Newcastle upon Tyne NE1 7RU, United Kingdom; [e]Department of Nuclear Science and Engineering, Massachusetts Institute of Technology, Cambridge, MA 02139; [f]Physicochimie des Electrolytes et Nanosystèmes interfaciaux Laboratory, CNRS and University Pierre et Marie Curie, 75252 Paris cedex 5, France; [g]Centre Interdisciplinaire de Nanoscience de Marseille, CNRS and Aix-Marseille University, 13288 Marseille cedex 09, France; and [h]Department of Physics and Institute for Soft Matter Synthesis and Metrology, Georgetown University, Washington, DC 20057

Edited by David A. Weitz, Harvard University, Cambridge, MA, and approved December 30, 2015 (received for review October 29, 2015)

Strength and other mechanical properties of cement and concrete rely upon the formation of calcium–silicate–hydrates (C–S–H) during cement hydration. Controlling structure and properties of the C–S–H phase is a challenge, due to the complexity of this hydration product and of the mechanisms that drive its precipitation from the ionic solution upon dissolution of cement grains in water. Departing from traditional models mostly focused on length scales above the micrometer, recent research addressed the molecular structure of C–S–H. However, small-angle neutron scattering, electron-microscopy imaging, and nanoindentation experiments suggest that its mesoscale organization, extending over hundreds of nanometers, may be more important. Here we unveil the C–S–H mesoscale texture, a crucial step to connect the fundamental scales to the macroscale of engineering properties. We use simulations that combine information of the nanoscale building units of C–S–H and their effective interactions, obtained from atomistic simulations and experiments, into a statistical physics framework for aggregating nanoparticles. We compute small-angle scattering intensities, pore size distributions, specific surface area, local densities, indentation modulus, and hardness of the material, providing quantitative understanding of different experimental investigations. Our results provide insight into how the heterogeneities developed during the early stages of hydration persist in the structure of C–S–H and impact the mechanical performance of the hardened cement paste. Unraveling such links in cement hydrates can be groundbreaking and controlling them can be the key to smarter mix designs of cementitious materials.

cement | microstructure | simulations | mesoscale | mechanics

Upon dissolution of cement powder in water, calcium–silicate–hydrates (C–S–H) precipitate and assemble into a cohesive gel that fills the pore space in the cement paste over hundreds of nanometers and binds the different components of concrete together (1). The mechanics and microstructure are key to concrete performance and durability, but the level of understanding needed to design new, more performant cements and have an impact on the CO_2 footprint of the material is far from being reached (2).

Most of the experimental characterization and models used to predict and design cement performance have been developed at a macroscopic level and hardly include any material heterogeneity over length scales smaller than micrometers (3). However, EM imaging, nanoindentation tests, X-rays and neutron scattering, and NMR analysis as well as atomistic simulations have now elucidated several structural and mechanical features concentrated within a few nanometers (4–8). The hygrothermal behavior of cement suggests a hierarchical and complex pore structure that develops during hydration and continues to evolve (1, 9–11). NMR and small-angle neutron scattering (SANS) studies of hardened C–S–H identified distinctive features of the complex pore network and detected significant structural heterogeneities spanning length scales between tens and hundreds of nanometers (12–14). Nanoindentation experiments have highlighted structural and mechanical heterogeneities over the same length scales (15). Their findings suggested that the internal stresses developed over those length scales during setting may be responsible for delayed nonlinear deformations, such as creep, that ultimately lead to major obstacles when designing the material properties and controlling the durability. Despite these advancements, the link between the nanoscale observations and the macroscale models currently used to predict and design cement performance is missing. Hence, to match the experimental observations, those models use ad hoc assumptions that cannot be independently tested or validated. Providing new quantitative information on the mesoscale texture of cement hydrates and how it may impact the material properties is the conundrum.

Here, we use a statistical physics approach to gain insight into the C–S–H at the scale of hundreds of nanometers based on the knowledge developed at the nanoscale. In our model, the complex pore network and the structural heterogeneities naturally emerge from the short-range cohesive interactions typical of nanoscale cement hydrates and the nonequilibrium conditions under which C–S–H densifies during cement setting. The scattering intensity, pore size distribution (PSD), surface area, local volume fractions, indentation modulus, and hardness measured in the simulations are compared with experiments and provide a first, to our knowledge, consistent characterization of the elusive mesoscale structure of C–S–H.

Significance

Calcium–silicate–hydrate (C–S–H) nanoscale gels are the main binding agent in cement and concrete, crucial for the strength and the long-term evolution of the material. Even more than the molecular structure, the C–S–H mesoscale amorphous texture over hundreds of nanometers plays a crucial role for material properties. We use a statistical physics framework for aggregating nanoparticles and numerical simulations to obtain a first, to our knowledge, quantitative model for such a complex material. The extensive comparison with experiments ranging from small-angle neutron scattering, SEM, adsorption/desorption of N_2, and water to nanoindentation provides new fundamental insights into the microscopic origin of the properties measured.

Author contributions: K.I., S.Y., F.-J.U., R.J.-M.P., and E.D.G. designed research; K.I., K.J.K., and C.G.H. performed research; K.I., M.B., E.M., and P.L. contributed new reagents/analytic tools; K.I., K.J.K., M.B., C.G.H., E.M., and P.L. analyzed data; and K.I., F.-J.U., P.L., R.J.-M.P., and E.D.G. wrote the paper.

The authors declare no conflict of interest.

This article is a PNAS Direct Submission.

Freely available online through the PNAS open access option.

[1]To whom correspondence may be addressed. Email: emanuela.del.gado@georgetown.edu or pellenq@mit.edu.

This article contains supporting information online at www.pnas.org/lookup/suppl/doi:10.1073/pnas.1520487113/-/DCSupplemental.

ENGINEERING

Results

In our coarse-grained model for cement hydrates, nanoscale units interact through a short-range attractive potential, prototypical of cement hydrates (16). The units (or particles) are the nanoscale cement hydrates identified in SANS measurements (4, 17). To mimic the continuous densification of the C–S–H gel, we combined molecular dynamics (MD) simulations of the interacting nanoscale units with a Grand Canonical Monte Carlo (GCMC) scheme, in which the free energy gain associated to the production of the cement hydrates and the attractive interactions between the nanoscale units drive the aggregation and increase of the density. These nonequilibrium simulations capture a few fundamental features of the kinetics of cement hydration at early stages (18, 19). Here, they have been used to produce C–S–H model structures at different stages of cement setting, corresponding to different values of the attained density (*Materials and Methods*). As a measure of the density, we use the packing fraction η, the total fraction of the simulation box volume occupied by the particles, where each particle i of linear size σ_i occupies a volume roughly $\simeq \pi/6\sigma_i^3$ (the range of particle sizes considered here has been chosen on the basis of the experimental information available) (13, 17) (*Materials and Methods* and *SI Appendix*).

The structural analysis of the simulation results reveals a rich morphology and provides novel insight into several experimental data. Fig. 1 shows the structures obtained for $\eta = 0.33$ and $\eta = 0.52$ and their characterization (*Materials and Methods*). The PSDs plotted in Fig. 1*A* show that nanopores in the range 0–3 nm (the gel pores in the cement literature) represent a significant contribution to the overall porosity of the gel (1). The data also clearly indicate mesopores of 3–30 nm, the capillary pores extensively discussed in the context of cement transport properties. Fig. 1*B* shows a representative pore structure at $\eta = 0.52$, with a complex pore network. The vast majority of the pores are connected, with a small amount of nanopores being isolated, which has great implications in terms of transport properties of confined fluids (electrolytes) for cement paste durability. As a result of the particle aggregation and the progressive densification of the gel, the population of nanopores and mesopores depends on the overall packing fraction: the lower the η value, the more abundant the mesopores, whereas the nanopores are more abundant as η increases. The PSDs shown here feature all important characteristics obtained in different experiments ranging from N_2 adsorption/desorption to NMR (1, 9, 20, 21). The quantitative comparison of the PSDs in Fig. 1*A* with the experiments of N_2 adsorption/desorption of ordinary Portland cement (OPC) samples prepared at different water-to-cement (w/c) ratio (9, 22) suggests that our samples with $\eta = 0.52$ could correspond to a cement paste prepared at w/c $\simeq 0.45$. After this correspondence, the samples at $\eta = 0.33$ could then be thought of as representative of C–S–H in a cement paste prepared with w/c >0.45 (i.e., larger than the minimum amount of water required for a full dissolution/precipitation of all of the clinker grain) (1). Hence, our results also support the idea that the excess of water during hydration (with respect to the 0.4 value) leads to a larger amount of mesopores, which was, indeed, measured (in terms of evaporable water) in the pioneering work by Powers and Brownyard (20) that is sketched in Fig. 1*C* (adapted from ref. 23) (C indicates a capillary pore).

The statistical analysis of local packing fraction η_{local} (*Materials and Methods*) reveals sizeable changes with the total packing fraction. Not only the solid material produced on aggregation and densification is structurally heterogeneous over these length scales, but also, the degree of heterogeneity varies at different stages of the setting process and for different w/c ratios of the cement paste. The distributions of the local packing fractions for $\eta = 0.33$ and $\eta = 0.52$ are plotted in Fig. 1*D* and display a distorted Gaussian shape with maximum values at $\eta_{local} = 0.45$ (for the samples with $\eta = 0.33$) and $\eta_{local} = 0.68$ (for $\eta = 0.52$). Nanoindentation tests have, indeed, detected significant variations of the local density in hardened C–S–H pastes (15), although most of the experiments reported values >0.55 for η_{local}. The data in Fig. 1*D* allow us to quantitatively connect to the classic work by Powers and Brownyard (20) based on the

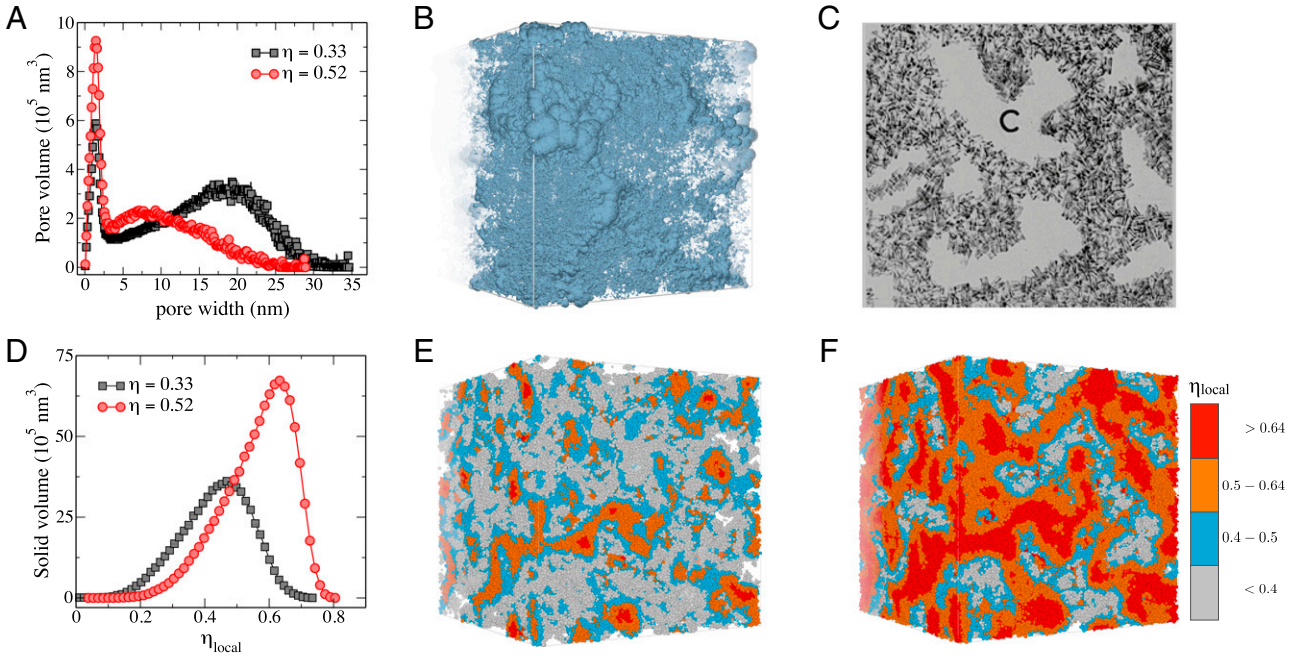

Fig. 1. (*A*) PSDs for $\eta = 0.33$ and $\eta = 0.52$. (*B*) Close-up view of the pore network for a sample with porosity $\phi = 0.48$, where $\phi = 1 - \eta$. The box size is $L = 195.22$ nm. (*C*) 2D schematic view of C–S–H. Reprinted from ref. 23. (*D*) Local volume fraction distributions η_{local} for $\eta = 0.33$ and $\eta = 0.52$. (*E*) Snapshot of a sample with $\eta = 0.33$ and (*F*) snapshot of a sample with $\eta = 0.52$ (the colors indicate η_{local} and $L = 585.54$ nm).

idea that the volume fraction of the mesopores (the capillary volume) found in the hardened, fully hydrated paste gives an indication of the initial w/c ratio. The maxima of η_{local} in Fig. 1*D* can be used to estimate the porosity of the densest domains (or volume fraction of the gel pores). The resulting volume fraction of the capillary pores, estimated as η/η_{max}, is in agreement with recent X-ray tomographic experiments (24) and would give, according to the work by Powers and Brownyard (20), w/c $\simeq 0.45$ for $\eta = 0.52$ and w/c $\simeq 0.7$ for $\eta = 0.33$, in line with the values obtained from the PSDs. Fig. 1 *E* and *F* illustrates the spatial distribution of the domains of different local packing fractions, showing two representative snapshots obtained for the two different values of η. It is interesting to see that the strands of the C–S–H dense gel, separated by capillary pores, are made of a continuous distribution of packing fractions of the polydisperse C–S–H nanoscale units. For $\eta = 0.52$, the densest regions span the whole sample as in a percolation network, suggesting that this part of the material dominates the mechanical response and hence, the results of nanoindentation tests. The spatial organization of the dense domains is strikingly reminiscent of the first models of C–S–H in the work by Powers (23) (Fig. 1*C*). In our simulations, such texture naturally emerges from the interactions and the nonequilibrium conditions that drive the densification of the material during cement hydration: because the structure of the gel grows in space and progressively densifies, the densest domains are in the backbone core of the interconnected gel strands covered by layers of gradually less dense material toward the surface of capillary pores (*SI Appendix*). This trend is more pronounced with increasing overall packing fraction.

The structures from the simulations can be compared with small-angle X-ray scattering (SAXS) or SANS data, which are extensively used to characterize and infer texture properties of hardened cement pastes (4, 14, 17, 25–27). In Fig. 2*A*, we plot the scattering intensity computed from the simulation data (*Materials and Methods*) for $\eta = 0.33$ and $\eta = 0.52$ and the SANS data from ref. 28. Apart from the lowest wave vectors (where the simulations data are limited by the system size), the curves can be readily compared, having considered that the calculations are in real physical units but that the signals are not expected to match exactly because of the presence of other hydration products in the experiments (e.g., ettringite, Portlandite, etc.) as opposed to the pure C–S–H of the simulations. At large q values (i.e., $q > 1$ nm^{-1}), we find, in agreement with experiments, a dependence $I(q) \sim q^{-4}$ typical of a Porod regime (29), indicating that the C–S–H surfaces have a subnanometric roughness (30). The Porod regime is followed at smaller q by the same q^{-3} dependence detected in the experiments that extends over more than one order of magnitude in length and that has been reported and discussed in the literature (4, 13, 27, 31). The ranges of wave vectors $q \simeq 0.07$–0.9 nm^{-1} indicate significant spatial correlations and heterogeneities over length scales between 3.5 and $\simeq 40$ nm, hence suggesting a prominent role of the mesopores in the SANS data. As in experiments (31), the q^{-3} dependence does not change on decreasing η (from 0.52 to 0.33) and hence, on increasing w/c. We have computed the length distributions of segments (chords) belonging to either the pores or the solid and having both ends on the interface (32). These stereological tools have been proven effective in characterizing porous media (33). Fig. 2*B* shows the in-pore chord-length distribution for our samples at $\eta = 0.33$ and $\eta = 0.52$ compared with that obtained from SEM images of a neat OPC paste in ref. 33 by assuming a pixel dimension of $\simeq 0.56$ nm in the experiments. At $\eta = 0.33$, our data reproduce particularly

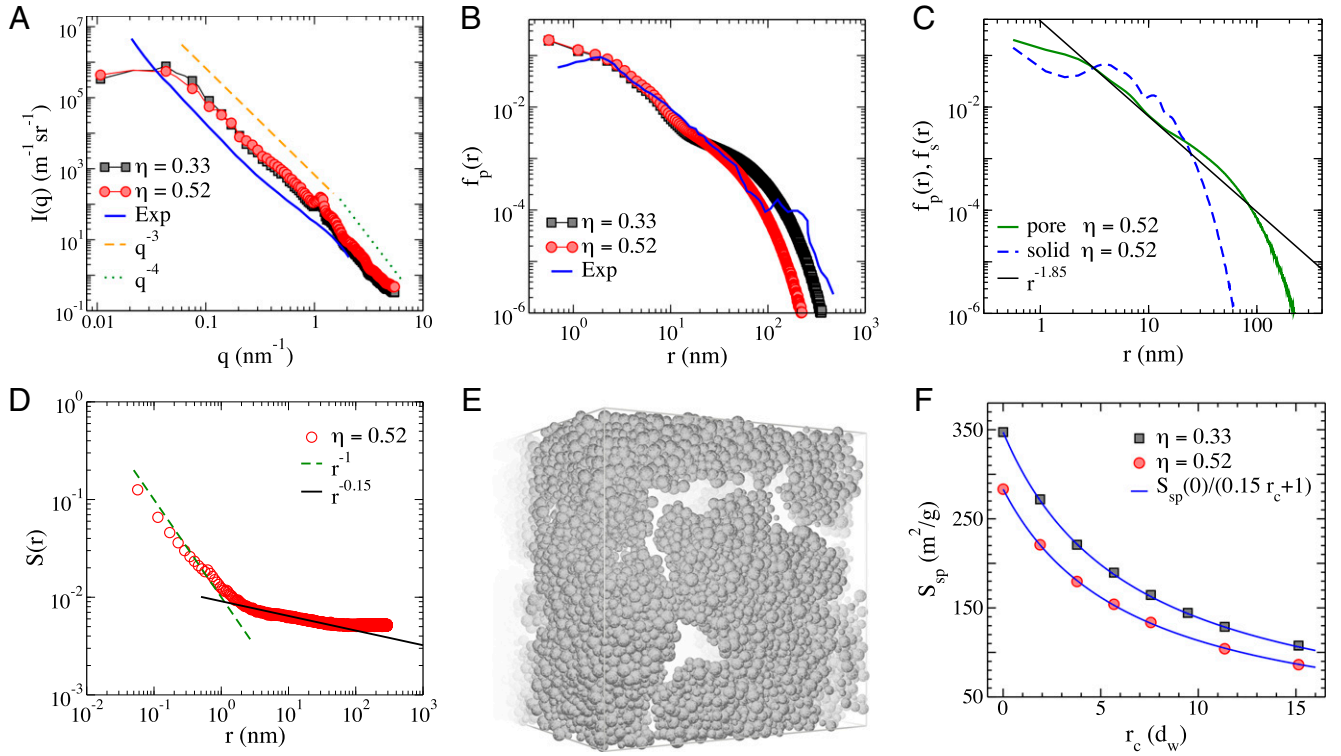

Fig. 2. (*A*) Scattering intensity for $\eta = 0.33$ and $\eta = 0.52$ from simulations and SANS data from ref. 28. (*B*) Pore chord-length distribution from simulations and SEM images in ref. 33. (*C*) Pore and solid chord-length distributions for $\eta = 0.52$. (*D*) Surface–surface correlation function for $\eta = 0.52$. (*E*) Close-up view of the solid from a snapshot at $\eta = 0.52$, where the surface roughness is shown (the box portion shown is $\simeq 195$ nm). (*F*) Specific surface area as a function of the cutoff distance of the pore chord-length distribution (the length unit is the water kinetic diameter $d_w = 0.3$ nm).

well the large chord-length values of the experimental curve. Both in-pore and in-solid chord-length distributions are compared in Fig. 2*C* for $\eta = 0.52$ (similar results are obtained for $\eta = 0.33$). In the range 3–40 nm, the in-pore chord-length distribution is close to an algebraic decay with an exponent $\simeq -1.85$, and, within $4-40$ nm, the in-solid one seems to follow the same decay. This result indicates that the mesopores are irregular in shape and/or have an irregular (rough) surface (34–36). Fig. 2*E* displays a section of the solid from a snapshot at $\eta = 0.52$, where the surface roughness can be appreciated. The spatial correlation of the chord length $S(r)$ is plotted as a function of the distance along the pore–solid interface in Fig. 2*D* for $\eta = 0.52$ (similar results are obtained for $\eta = 0.33$). The data show two distinct regimes: a $1/r$ dependence at short distances (because of the flat surface of the volume elements used to define the interface) and a much slower decay at larger distances $\sim r^{-0.15}$, indicating that, indeed, the interface is rough and that long-range spatial correlations are present. The data in Fig. 2 *C* and *D* suggest that surface correlations caused by the roughness become negligible beyond 40 nm, whereas the in-pore chords data and the scattering intensity indicate that pore sizes and spatial correlations, respectively, extend beyond 40 nm through a fractal distribution of pore volumes. Both the surface and in-pore chord data are consistent with a multiscale rough and porous structure (compatible with a fractal dimension $d_f \simeq 2.8-3$) (36). The emerging picture is that the extended q^{-3} regime in the scattering intensity of C–S–H is the result of a unique combination (among other porous materials) of the mesopores surface roughness and the complex (fractal) volume of the mesopore network.

From the in-pore chord-length distributions, knowing the packing fraction of the solid matrix η, we can extract the geometric-specific surface area of our samples as $S_{sp}^{geo} = 4\phi/[\rho_s(1-\phi)\langle l\rangle]$, where $\phi = 1-\eta$ is the global porosity, ρ_s is the density of C–S–H particles, and $\langle l\rangle$ is the first moment of the (normalized) chord-length distribution (33, 37). The specific surface area can be measured in adsorption/desorption experiments (10, 38, 39); $\rho_s \simeq 2.43$ g/mL is the density of the C–S–H nanoscale grains from atomistic simulations (5, 8). We use a lower-bound cutoff length r_c for the chord-length distribution, which, of course, modifies the measured value S_{sp}: neglecting pores, anfractuosity, and roughness sizes below r_c decreases the measured specific surface area. Hence, in Fig. 2*F*, we plot S_{sp} as a function of r_c and obtain S_{sp}^{geo} by extrapolating r_c to zero (i.e., probing the pore volume with the whole possible range of chord lengths). We find $S_{sp} \simeq S_{sp}^{geo}/(0.15\, r_c + 1)$, from which we obtain $S_{sp}^{geo} = 347$ m^2/g for $\eta = 0.33$ and $S_{sp}^{geo} = 283$ m^2/g for $\eta = 0.52$. These values are, by far, larger than those measured in adsorption experiments (1, 9, 11, 40, 41), reporting a wide range of S_{sp} values from 50 to 200 m^2/g, which depend on the initial w/c. Whereas it is well-established that adsorption experiments underestimate S_{sp}^{geo} by at least 20% (37, 42), the span of experimental data depending on the adsorbate (in most cases, nitrogen at 77 K and water at 300 K) is traditionally considered the result of C–S–H structure, because contrary to water, the nitrogen accesses only part of the porosity in C–S–H (typically not the layered nanotexture of C–S–H) (43). Indeed, the Jennings colloidal model (44, 45) assumes two local densities with pore features designed to justify the difference in water and N_2 measurements. The more complex scenario for pore structure and local densities emerging from our study suggests a different origin of the S_{sp} values. Recent studies (8, 46) point to differences in the drying conditions and have shown that, only in oven-dried C–S–H at 100 °C under vacuum, the water of all C–S–H pores (gel and capillary) is completely removed, leaving only water molecules in the nanotexture. In these conditions, the measured specific surface area of C–S–H (using water as an adsorption probe) is $S_{sp}^{H_2O} = 200-300$ m^2/g. These values, once increased by 20% to obtain S_{sp}^{geo}, are close to our estimate. A stable water layer (two-molecules thick), found in simulations and caused by ultra-hydrophilicity of C–S–H surface (47), can block the access of nitrogen to most C–S–H gel porosity when cooled down to 77 K for nitrogen adsorption/desorption experiments. Fig. 2*F* shows that, with an $r_c \simeq 3$ nm (i.e., roughly 10 water molecules, meaning that all anfractuosities and pores smaller than that size remain filled with water), we obtain specific surface values of 135 and 115 m^2/g for $\eta = 0.33$ and $\eta = 0.52$, respectively. We can attribute these values mainly to the specific surface of the large (capillary) mesopores, and subtracting them from the total specific surface, we get the contributions of the small nanopores, which are $\simeq 168$ and $\simeq 212$ m^2/g for $\eta = 0.52$ and $\eta = 0.33$, respectively. As a rule of thumb, the total specific surface area can be split in two contributions (gel vs. capillary): $S_{sp}^{tot} = \phi S_{sp}^{gel} + S_{sp}^{capillary}$, where $S_{sp}^{gel} \simeq 350$ m^2/g is the actual intrinsic specific surface area of the denser regions with volume fraction > 0.66. Hence, our data are consistent with the idea that most usual drying conditions hardly affect the cement nanotexture (9, 48), remaining largely hydrated (47), and the adsorption/desorption experiments only probe the large capillary pores, with amounts increasing with the initial w/c ratio.

Finally, we have performed nanoindentation experiments on hardened cement pastes to determine the nanoscale modulus M and hardness H of the material and measured the same properties in the samples obtained from the simulations (*Materials and Methods* and *SI Appendix*). In Fig. 3 *A* and *B*, we plot M and H as a function of η in experiments and simulations,

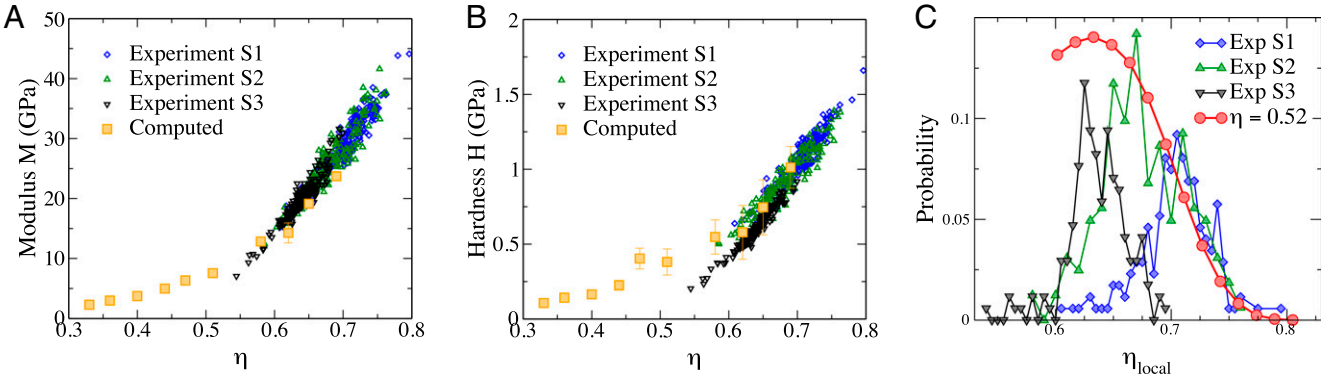

Fig. 3. (*A*) The C–S–H modulus M and (*B*) the hardness H as a function of η for simulations and experiments. (*C*) Local volume fractions with $\eta = 0.52$ from simulations compared with volume fractions of experimental samples S1–S3 from nanoindentation.

with excellent agreement. The packing fraction distribution obtained in experiments (*Materials and Methods* and *SI Appendix*) is compared with the distribution of η_{local} obtained in the model as shown in Fig. 3*C*. In these experiments, Portlandite and all other minor phases have been carefully excluded, and the data refer only to the C–S–H phase. For the three samples S1, S2, and S3, the experimental local volume fractions are in the range from 0.54 to 0.8, with a maximum value at η_{max} in the range from 0.62 to 0.7, which is in good agreement with values sampled in the densest domains of the model with $\eta = 0.52$. Note that all distributions in Fig. 3*C* are normalized and that the one obtained from the model for $\eta = 0.52$ is normalized in the range $0.6 - 0.8$. These densest regions form a connected, spanning cluster (*SI Appendix*), which is likely to dominate the mechanical properties of the material. The comparison of these data highlights the fact that nanoindentation experiments are mainly sensitive to the densest part ($\eta > 0.6$) of the material.

Discussion and Conclusion

In our results, a complex, extended pore network as well as a continuum distribution of local densities compose a physical picture of C–S–H beyond the classic colloidal model based on two distinct local densities (4, 44). Such complex morphology reconciles a number of different experiments ranging from SANS, chord-length analysis of SEM images, and specific surface area to nanoindentation hardness measurements to a consistent understanding. The mesoscale texture obtained here is consistent with adsorption/desorption experiments, NMR, and Powers–Brownyard classic relations estimating capillary and gel pores volumes. The intriguing q^{-3} behavior of the SANS signal observed experimentally over an unusually large range of distances is due to a unique coexistence of a surface roughness of the capillary pores with a complex (fractal) pore network, all consequences of the interplay between the cohesive nanoscale effective interactions and the out-of-equilibrium conditions in which the material forms during cement hydration. From the calculations of the specific surface area, we have formulated a new perspective on water and nitrogen adsorption experiments: drying conditions may determine which part of the pore population is accessible to the adsorbate, limiting the access to the nanoscale gel pores. Developing further, our findings are at odds with the idea that creep or drying shrinkage could be related to the rearrangement of the water in the subnanotexture of the material (49, 50) (in absence of harsh temperature conditions). Our study delivers for the first time, to our knowledge, a quantitative description of the mesoscale texture of C–S–H and opens the way to elaborating new, physically grounded constitutive models bridging from the nanoscale characterization of the material to its continuum description and its engineering applications (51–53).

Materials and Methods

Model for C–S–H. Simulations of C–S–H precipitation were performed using a hybrid scheme of GCMC and MD (18, 19) (*SI Appendix*). A GCMC cycle consists of N_{MC} attempts of particle insertion or deletion followed by N_{MD} = 100 MD steps in NVT (canonical) ensemble (*SI Appendix*). $R = N_{MC}/(N_{MD} \cdot L^3 \cdot \delta t)$, where L is the length of the simulation box and $\delta t = 0.0025\sqrt{m\sigma^2/\varepsilon}$, is the rate of hydrate production. In this work, $R = 25 \cdot 10^{-9} \delta t^{-1} nm^{-3}$. The effective interactions at late stages of cement hydration are modeled with a generalized Lennard–Jones potential $V(r) = 6\varepsilon[(\sigma/r)^{2\gamma} - (\sigma/r)^{\gamma}]$, where r is the interparticle distance, and ε is the strength of the attraction between two particles with diameter σ and $\gamma = 12$. The temperature was T = 0.15 and the chemical potential $\mu = -1$ in reduced units. The particle size σ was randomly distributed between 3.78 and 9.2 nm (*SI Appendix*). The simulations have been performed with box sizes L = 195.22, 390.36, and 585.54 nm with particles up to $6.1 \cdot 10^5$ and at least five independent samples for each L. The results refer to the largest systems unless otherwise stated.

Structural Properties. The PSDs were computed using the technique used in the work in ref. 54, where the pore size of a point in the void space is determined by the diameter of the largest sphere that does not overlap with the solid particles. The local packing fraction η_{local} was computed in a spherical region of radius 35 nm around each spherical particle i with radius $r_i = \sqrt[12]{2}\sigma_i$ (*SI Appendix*). For the small-angle scattering $I(q)$, we first generated a digitized 3D image of the structure with a voxel size of 0.571 nm, much smaller than the minimum particle diameter of 3.78 nm and well below the box size of 585.54 nm. Having computed the two-point fluctuation autocorrelation function $\eta^2(r)$, the $I(q)$ was deduced in absolute scale using the following relation: $I(q) = -[2\pi(\Delta\rho)^2/q][d(Re(\tilde{\eta}^2(q))/dq]$, where $\Delta\rho$ is the scattering length density contrast, and $\tilde{\eta}^2(q)$ is the 1D Fourier transform of $\eta^2(r)$ (36). We also computed $I(q)$ using the projection theorem (30) and the digitized projections of the 3D images in x, y, and z directions. Both computations were in good agreement. In both cases, special attention to finite size of the configuration box was taken. In Fig. 2*A*, the plateau at low wave vector q is associated to a correlation length of about $\pi/q = 40$ nm, 10 times smaller than the box size (585.54 nm). This correlation length is also the distance where the algebraic evolution of the two-point pore–solid interface correlation function $S(r)$ ends followed by a plateau at higher correlation distances (Fig. 2*D* and *SI Appendix*).

Mechanical Properties. The stiffness of the interaction between two particles of size σ is defined as the curvature of the generalized Lennard–Jones potential, and at the local equilibrium distance $r_m = \sqrt[12]{2}\sigma$, it equals $\varepsilon/(444\sigma^2)$. Assuming that the cohesive strength between particles is the same as for the calcium–silicate layers within a C–S–H grain, we express the interparticle stiffness as YA/r_m, where Y is the Young modulus of solid C–S–H [68.4 GPa from atomistic simulations of few nanometers of C–S–H grains (55)], and $A = \pi r_m^2$ is the cross-section of the applied force. All of this leads to a unit pressure $\varepsilon/\sigma^3 = 0.51$ GPa. The C–S–H configurations were relaxed to zero stress before computing indentation modulus M and hardness H. To compute M, we slightly deform the simulation box in the three axial directions and the three shear planes. The range of strain for the elastic deformation is ± 0.005. The indentation modulus M was computed as a linear combination of the bulk K and shear modulus G: $M = 4G(3K + G)/(3K + 4G)$ (56). The hardness H was computed as in the work in ref. 8, where the yield stress is quantified by using the 0.2% offset method. We performed simulations with monotonic increase of axial and shear strains by a series of box deformation–energy minimization steps (pure tension, simple shear, and three intermediate combinations of both). For each simulation, we draw a Mohr circle in the axial stress–shear stress plane representing the state of stress when the onset of failure is reached (57). The Mohr circle has a single tangent line that defines the strength envelope and is described by its shear stress intercept at zero axial stress (cohesion) and its gradient (friction angle). The cohesion and friction angle are used to compute H (58). M and H were computed for configurations with box size of 390.36 nm. Technical details are discussed in *SI Appendix*.

Experiments. Three cement paste specimens were investigated. The first specimen (S1) was synthesized using oil-well cement, class G and quartz hydrated at w/c = 0.43 for over 1 y. Specimens S2 and S3 were made with ordinary Portland cement type I (OPC CEM-I) and hydrated at room temperature with w/c = 0.35. The hydration reaction was stopped at 24 (S2) and 17 (S3) h with the solvent exchange method (59). The S3 sample also contained C–S–H seeds. Force-controlled nanoindentation tests were performed to a maximum indentation depth of 300 nm, with a linear loading and unloading rate of 12 mN/min and a dwell time of 5 s (60, 61). M and H were calculated from the raw curves (62, 63). The indentation results were linked together with chemistry information of Ca, Si, Al, and Fe acquired by backscattered images and elemental maps using an image-processing algorithm to assure one-to-one spatial correlation (60). The packing fraction distribution of the C–S–H gel is then determined following the micromechanics approach (64–66) by isolating C–S–H in the coupled indentation–chemistry analysis assuming C–S–H particle stiffness to be 72 ± 3 GPa (8). Technical details are discussed in *SI Appendix*.

ACKNOWLEDGMENTS. This work is supported by Schlumberger under the Cement under Extreme Conditions Project and the Concrete Sustainability Hub at Massachusetts Institute of Technology. E.D.G. acknowledges support from Swiss National Science Foundation Grant PP00P2_150738 and National Science Foundation Grant NSF PHY11-25915. This work has been carried out within the framework of ICoME2 Labex Project ANR-11-LABX-0053 and A*MIDEX Project ANR-11-IDEX-0001-02 cofunded by the French program Investissements d'Avenir, which is managed by the French National Research Agency.

1. Taylor HF (1997) *Cement Chemistry* (Thomas Telford, London).
2. Boden T, Marland G, Andres R (2012) *Global, Regional, and National Fossil-Fuel CO2 Emissions* (Carbon Dioxide Information Analysis Center, Oak Ridge National Laboratory and US Department of Energy, Oak Ridge, TN).
3. Thomas J, et al. (2011) Modeling and simulation of cement hydration kinetics and microstructure development. *Cement Concr Res* 41(12):1257–1278.
4. Allen AJ, Thomas JJ, Jennings HM (2007) Composition and density of nanoscale calcium-silicate-hydrate in cement. *Nat Mater* 6(4):311–316.
5. Pellenq RJM, et al. (2009) A realistic molecular model of cement hydrates. *Proc Natl Acad Sci USA* 106(38):16102–16107.
6. Vandamme M, Ulm FJ, Fonollosa P (2010) Nanogranular packing of C–S–H at substochiometric conditions. *Cement Concr Res* 40(1):14–26.
7. Richardson I (2008) The calcium silicate hydrates. *Cement Concr Res* 38(2):137–158.
8. Abdolhosseini Qomi MJ, et al. (2014) Combinatorial molecular optimization of cement hydrates. *Nat Commun* 5(2014):4960.
9. Mikhail RS, Copeland LE, Brunauer S (1964) Pore structures and surface areas of hardened portland cement pastes by nitrogen adsorption. *Can J Chem* 42(2):426–438.
10. Ranaivomanana H, Verdier J, Sellier A, Bourbon X (2011) Toward a better comprehension and modeling of hysteresis cycles in the water sorption–desorption process for cement based materials. *Cement Concr Res* 41(8):817–827.
11. Baroghel-Bouny V, Mainguy M, Lassabatere T, Coussy O (2007) Characterization and identification of equilibrium and transfer moisture properties for ordinary and high-performance cementitious materials. *Cement Concr Res* 29(8):1225–1238.
12. Barberon F, Korb JP, Petit D, Morin V, Bermejo E (2003) Probing the surface area of a cement-based material by nuclear magnetic relaxation dispersion. *Phys Rev Lett* 90(11):116103.
13. Brisard S, et al. (2012) Morphological quantification of hierarchical geomaterials by X-ray nano-CT bridges the gap from nano to micro length scales. *Am Mineral* 97: 480–483.
14. Allen AJ, Thomas JJ (2007) Analysis of C-S-H gel and cement paste by small-angle neutron scattering. *Cement Concr Res* 37(3):319–324.
15. Constantinides G, Ulm FJ (2007) The nanogranular nature of C–S–H. *J Mech Phys Solids* 55(1):64–90.
16. Pellenq RJM, Van Damme H (2004) Why does concrete set?: The nature of cohesion forces in hardened cement-based materials. *MRS Bull* 29(05):319–323.
17. Chiang WS, Fratini E, Baglioni P, Liu D, Chen SH (2012) Microstructure determination of calcium-silicate-hydrate globules by small-angle neutron scattering. *J Phys Chem C Nanomater Interfaces* 116(8):5055–5061.
18. Ioannidou K, Pellenq RJM, Del Gado E (2014) Controlling local packing and growth in calcium-silicate-hydrate gels. *Soft Matter* 10(8):1121–1133.
19. Del Gado E, et al. (2014) A soft matter in construction—Statistical physics approach to formation and mechanics of C–S–H gels in cement. *Eur Phys J Spec Top* 223(11): 2285–2295.
20. Powers TC, Brownyard TL (1946) Studies of the physical properties of hardened Portland cement paste. *American Concrete Institute Journal Proceedings* 43(9): 249–336.
21. Valckenborg R, Pel L, Kopinga K (2002) Combined NMR cryoporometry and relaxometry. *J Phys D Appl Phys* 35(3):249–256.
22. Rouquerol F, Rouquerol J, Sing K (1999) *Adsorption by Powders and Solids: Principles, Methodology, and Applications* (Academic, London).
23. Powers TC (1958) Structure and physical properties of hardened portland cement paste. *J Am Ceram Soc* 41(1):1–6.
24. da Silva JC, et al. (2015) Mass density and water content of saturated never-dried calcium silicate hydrates. *Langmuir* 31(13):3779–3783.
25. Allen AJ, McLaughlin JC, Neumann DA, Livingston RA (2004) situ quasi-elastic scattering characterization of particle size effects on the hydration of tricalcium silicate. *J Mater Res* 19(11):3242–3254.
26. Fratini E, Faraone A, Ridi F, Chen SH, Baglioni P (2013) Hydration water dynamics in tricalcium silicate pastes by time-resolved incoherent elastic neutron scattering. *J Phys Chem C Nanomater Interfaces* 117(14):7358–7364.
27. Bae S, et al. (2015) Soft X-ray ptychographic imaging and morphological quantification of calcium silicate hydrates (C–S–H). *J Am Ceram Soc* 98(12):4090–4095.
28. Krakowiak KJ, et al. (2015) Nano-chemo-mechanical signature of conventional oil-well cement systems: Effects of elevated temperature and curing time. *Cement Concr Res* 67:103–121.
29. Guinier A, Fournet G (1955) *Small-Angle Scattering of X-Rays* (Wiley, New York).
30. Brisard S, Levitz P (2013) Small-angle scattering of dense, polydisperse granular porous media: Computation free of size effects. *Phys Rev E Stat Nonlin Soft Matter Phys* 87(1):013305.
31. Aldridge L, et al. (1994) *Small-Angle Neutron Scattering from Hydrated Cement Pastes* (Cambridge Univ Press, Cambridge, United Kingdom), Vol 376, p 471.
32. Mering J, Tchoubar D (1968) Interprétation de la diffusion centrale des rayons X par les systemes poreux. I. *J Appl Crystallogr* 1(3):153–165.
33. Levitz P (1998) Off-lattice reconstruction of porous media: Critical evaluation, geometrical confinement and molecular transport. *Adv Colloid Interface Sci* 76:71–106.
34. Bale HD, Schmidt PW (1984) Small-angle X-ray-scattering investigation of submicroscopic porosity with fractal properties. *Phys Rev Lett* 53(6):596.
35. Vicsek T (1992) *Fractal Growth Phenomena* (World Scientific, Teaneck, NJ), Vol 2.
36. Levitz P, Tchoubar D (1992) Disordered porous solids: From chord distributions to small angle scattering. *J Phys I* 2(6):771–790.
37. Pellenq RM, Levitz P (2002) Capillary condensation in a disordered mesoporous medium: A grand canonical monte carlo study. *Mol Phys* 100(13):2059–2077.
38. Maruyama I, Nishioka Y, Igarashi G, Matsui K (2014) Microstructural and bulk property changes in hardened cement paste during the first drying process. *Cement Concr Res* 58:20–34.
39. Wu M, Johannesson B, Geiker M (2014) A study of the water vapor sorption isotherms of hardened cement pastes: Possible pore structure changes at low relative humidity and the impact of temperature on isotherms. *Cement Concr Res* 56:97–105.
40. Bye GC, Chigbo GO (1973) Ageing of some high surface area solids. *J Chem Technol Biotechnol* 23(8):589–599.
41. Thomas JJ, Jennings HM, Allen AJ (1998) The surface area of cement paste as measured by neutron scattering: Evidence for two CSH morphologies. *Cement Concr Res* 28(6):897–905.
42. Coasne B, Gubbins KE, Pellenq RJM (2004) A grand canonical monte carlo study of adsorption and capillary phenomena in nanopores of various morphologies and topologies: Testing the BET and BJH characterization methods. *Part Part Syst Charact* 21(2):149–160.
43. Feldman RF (1973) Helium flow characteristics of rewetted specimens of dried hydrated portland cement paste. *Cement Concr Res* 3(6):777–790.
44. Jennings HM (2008) Refinements to colloid model of CSH in cement: CM-II. *Cement Concr Res* 38(3):275–289.
45. Jennings HM, Kumar A, Sant G (2015) Quantitative discrimination of the nano-pore-structure of cement paste during drying: New insights from water sorption isotherms. *Cement Concr Res* 76:27–36.
46. Suda Y, Saeki T, Saito T (2015) Relation between chemical composition and physical properties of CSH generated from cementitious materials. *J Adv Concr Technol* 13(5): 275–290.
47. Levitz P, Bonnaud P, Cazade PA, Pellenq RM, Coasne B (2013) Molecular intermittent dynamics of interfacial water: Probing adsorption and bulk confinement. *Soft Matter* 9(36):8654–8663.
48. Zhang J, Weissinger EA, Peethamparan S, Scherer GW (2010) Early hydration and setting of oil well cement. *Cement Concr Res* 40(7):1023–1033.
49. Bažant ZP, Hauggaard AB, Baweja S, Ulm FJ (1997) Microprestress solidification theory for concrete creep. I: Aging and drying effects. *J Eng Mech* 123(11):1188–1194.
50. Pinson MB, et al. (2015) Hysteresis from multiscale porosity: Modeling water sorption and shrinkage in cement paste. *Phys Rev Appl* 3(6):064009.
51. Pichler B, Hellmich C (2011) Upscaling quasi-brittle strength of cement paste and mortar: A multi-scale engineering mechanics model. *Cement Concr Res* 41(5):467–476.
52. Pichler B, et al. (2013) Effect of gel–space ratio and microstructure on strength of hydrating cementitious materials: An engineering micromechanics approach. *Cement Concr Res* 45:55–68.
53. Bentz DP, Jones SZ, Snyder KA (2015) Design and performance of ternary blend high-volume fly ash concretes of moderate slump. *Construct Build Mater* 84:409–415.
54. Bhattacharya S, Gubbins KE (2006) Fast method for computing pore size distributions of model materials. *Langmuir* 22(18):7726–7731.
55. Manzano H, et al. (2012) Confined water dissociation in microporous defective silicates: Mechanism, dipole distribution, and impact on substrate properties. *J Am Chem Soc* 134(4):2208–2215.
56. Masoero E, Del Gado E, Pellenq RJM, Yip S, Ulm FJ (2014) Nanoscale mechanics of colloidal C-S-H gels. *Soft Matter* 10(3):491–499.
57. Holtz RD, Kovacs WD (1981) *An Introduction to Geotechnical Engineering* (Prentice Hall, Englewood Cliffs, NJ).
58. Ganneau F, Constantinides G, Ulm FJ (2006) Dual-indentation technique for the assessment of strength properties of cohesive-frictional materials. *Int J Solids Struct* 43(6):1727–1745.
59. Zhang J, Scherer GW (2011) Comparison of methods for arresting hydration of cement. *Cement Concr Res* 41(10):1024–1036.
60. Krakowiak KJ, Wilson W, James S, Musso S, Ulm FJ (2015) Inference of the phase-to-mechanical property link via coupled X-ray spectrometry and indentation analysis: Application to cement-based materials. *Cement Concr Res* 67:271–285.
61. Miller M, Bobko C, Vandamme M, Ulm FJ (2008) Surface roughness criteria for cement paste nanoindentation. *Cement Concr Res* 38(4):467–476.
62. Oliver W, Pharr G (1992) An improved technique for determining hardness and elastic modulus using load and displacement sensing indentation experiments. *J Mater Res* 7(06):1564–1583.
63. Oliver W, Pharr G (2004) Measurement of hardness and elastic modulus by instrumented indentation: Advances in understanding and refinements to methodology. *J Mater Res* 19(01):3–20.
64. Ulm FJ, et al. (2007) Statistical indentation techniques for hydrated nanocomposites: Concrete, bone, and shale. *J Am Ceram Soc* 90(9):2677–2692.
65. Bobko C, et al. (2011) The nanogranular origin of friction and cohesion in shale—A strength homogenization approach to interpretation of nanoindentation results. *Int J Numer Anal Methods Geomech* 35:1854–1876.
66. Cariou S, Ulm FJ, Dormieux L (2008) Hardness and packing density scaling relations for cohesive-frictional porous materials. *J Mech Phys Solids* 56(3):924–952.